npj computational materials

www.nature.com/npjcompumats

ARTICLE OPEN

Check for updates

Shift current response in elemental two-dimensional ferroelectrics

Zhuang Qian[1,2], Jian Zhou[3], Hua Wang[1] and Shi Liu[2,4]✉

A bulk material without inversion symmetry can generate a direct current under illumination. This interface-free current generation mechanism, referred to as the bulk photovoltaic effect (BPVE), does not rely on *p-n* junctions. Here, we explore the shift current generation, a major mechanism responsible for the BPVE, in single-element two-dimensional (2D) ferroelectrics represented by phosphorene-like monolayers of As, Sb, and Bi. The strong covalency, small band gap, and large joint density of states afforded by these elemental 2D materials give rise to large shift currents, outperforming many state-of-the-art materials. We find that the shift current, due to its topological nature, depends sensitively on the details of the Bloch wave functions. It is crucial to consider the electronic exchange-correlation potential beyond the generalized gradient approximation as well as the spin-orbit interaction in density functional theory calculations to obtain reliable frequency-dependent shift current responses.

npj Computational Materials (2023)9:67 ; https://doi.org/10.1038/s41524-023-01026-3

INTRODUCTION

High-performing photoelectric conversion is essential to the solar cell technology. Traditional photovoltaic cells based on *p-n* junctions need the built-in electric field at the interface to separate electron-hole pairs and the efficiency is constrained by the Shockley–Queisser limit[1]. The bulk photovoltaic effect (BPVE) is the direct conversion of solar energy into direct current (DC), which has been considered as a promising alternative source of photocurrent[2–7]. As the name suggests, the presence of the BPVE does not require a complicated interface that often demands precisely controlled heterostructure fabrication process to minimize unwanted impurities and electric resistance. Single-phase bulk materials with broken inversion symmetry can generate steady photocurrent and above-band-gap photovoltage under uniform illumination in the absence of external bias[8–12], potentially enabling the implementation of the whole bulk material for photoelectric conversion[13–16].

In the clean limit, the BPVE response can be obtained from the quadratic response theory using the density matrix method[17,18] or from the perspective of divergent susceptibilities[19–21] where the light is treated as a classical electromagnetic field interacting with Bloch electrons. Ferroelectrics intrinsically exhibit the BPVE because of the fundamental requirement of spontaneous inversion symmetry breaking. Shift current is one of the most important mechanisms responsible for the BPVE[22–24], and was first observed in ferroelectrics experimentally[25]. As a zero-bias topological photocurrent[26,27], shift current is intimately related to the change in the phases of Bloch wave functions during the photoexcitation of an electron from the valence to the conduction band[28]. A large shift current is desirable for photoelectric conversion. Previous experimental and theoretical investigations of shift current in a wide range of noncentrosymmetric materials systems such as bulk perovskite ferroelectrics[29–32], two-dimensional (2D) materials[33–38], nanotubes[39], conjugated polymers[40], and topological insulators[41–45] have led to two general design principles for enhancing the current density. First, low-dimensional materials with large joint density of states (JDOS) tend to present large shift current responses upon photoexcitation[46]. The delocalization of electronic states is another important parameter that affects the shift current magnitude, and covalently bonded materials characterized by large long-range electron hopping amplitudes could give rise to large shift currents[6,29,40].

Recently, a family of phosphorene-like 2D elemental group-V (As, Sb, and Bi) monolayers was predicted to possess spontaneous switchable in-plane polarization[47] arising from the out-of-plane atomic-layer buckling. We propose that single-element 2D ferroelectrics are promising candidates to support large shift currents because of the strong covalency intrinsic to the homoelement bonding and pronounced singularities in the density of states common to 2D materials. In this work, we explore the shift current in these newly predicted elemental ferroelectrics with density functional theory (DFT) calculations and find that they can generate large shift currents over a wide range of wavelengths including the visible light spectrum. In addition, our work highlights the importance of spin-orbit coupling (SOC) and electronic correlation effect on the shift current spectrum even in 2D systems containing light elements.

RESULTS AND DISCUSSION

Structure

The structure of single-element group-V monolayer is displayed in Fig. 1. The puckered lattice structure without centrosymmetry (space group $Pmn2_1$) can be viewed as a distorted phosphorene-like structure. The out-of-plane atomic buckling causes charge accumulations at the outmost group-V atoms, leading to spontaneous in-plane polarization along the *y* axis[47]. We compute the Born effective charges (see inset table in Fig. 1) and confirm the buckling-induced charge accumulation/depletion mechanism. The dynamic stability of ferroelectric group-V monolayer has been confirmed by the computed phonon spectrum that has no imaginary phonon

[1]Zhejiang University, Hangzhou, Zhejiang 310058, China. [2]Key Laboratory for Quantum Materials of Zhejiang Province, Department of Physics, School of Science and Research Center for Industries of the Future, Hangzhou, Zhejiang 310030, China. [3]Center for Alloy Innovation and Design, State Key Laboratory for Mechanical Behavior of Materials, Xi'an Jiaotong University, Xi'an 710049, China. [4]Institute of Natural Sciences, Westlake Institute for Advanced Study, Hangzhou, Zhejiang 310024, China. ✉email: liushi@westlake.edu.cn

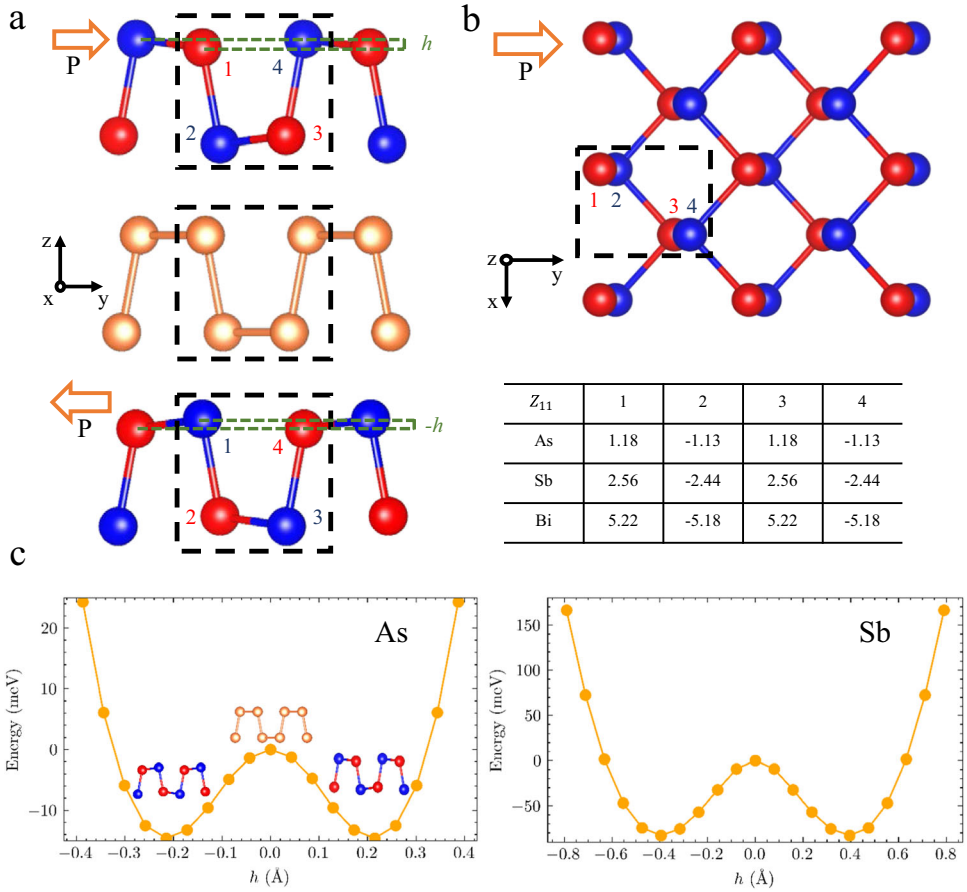

Z_{11}	1	2	3	4
As	1.18	-1.13	1.18	-1.13
Sb	2.56	-2.44	2.56	-2.44
Bi	5.22	-5.18	5.22	-5.18

Fig. 1 Ferroelectric single-element group-V monolayers. Schematics of **a** side view and **b** top view of crystal structures of single-element group-V monolayer with in-plane polarization along the *y* axis. The inversion symmetry breaking results from the spontaneous atomic layer buckling denoted as *h*. The atoms are colored based on the sign of the Born effective charge (Z_{11}) reported in the table (blue for negative and red for positive). **c** Energy evolution as a function of buckling height *h* in monolayer As monolayer (left) and monolayer Sb (right), revealing a double well potential.

modes over the whole Brillouin zone[47]. Xu et al. recently simulated the polarization-electric field hysteresis loop for monolayer As[48], and the predicted in-plane spontaneous polarization is 0.42×10^{-10} C/m, comparable with ferroelectric monolayer SnTe[49]. We compute the energy evolution as a function of buckling parameter *h* (Fig. 1a) in monolayer As and Sb, respectively, each revealing a double well potential landscape, typical for a ferroelectric phase (Fig. 1c). It is worth noting that group-V monolayers, similar to phosphorene, have already been experimentally synthesized for Sb and Bi[50–52]. We only consider in-plane shift currents (σ^{xbc} and σ^{ybc}) in this work. Since the mirror symmetry $\mathcal{M}_x : x \to -x$ leaves the monolayer invariant, only three components of the response tensor, σ^{yxx}, σ^{yyy}, and σ^{yzz}, can be nonzero due to the symmetry constraint that holds at any photon frequency. Here, we focus on the responses under incident light perpendicular to the 2D sheet, namely, σ^{yxx} and σ^{yyy}.

Monolayer arsenic

The DFT band structures and the corresponding shift current spectra for monolayer As computed with PBE, PBE+SOC, HSE, and HSE+SOC are presented in Fig. 2, revealing several intriguing features. The band gap predicted by PBE is 0.15 eV, and the peak in the σ^{yyy} spectrum exceeds 1000 μA/V^2 for photon energies near the band edge. In comparison, HSE predicts a larger band gap of 0.47 eV, whereas the peak value of σ^{yyy} drops considerably to only 150 μA/V^2. Similarly, the band-edge value of σ^{yxx} estimated by PBE is >3000 μA/V^2 but the HSE predicts a much smaller value of 250 μA/V^2. Such pronounced reduction in the peak response is unexpected as the HSE band structure looks like a rigid shift of the PBE band structure without substantial changes in the band dispersions. This highlights the importance of treating the exchange-correlation potential beyond the semilocal approximation in DFT calculations.

Moreover, the inclusion of the SOC effect, though inducing little impact on the band gap, causes drastic changes in the shift current spectra for both PBE and HSE. At the PBE level, the band gap reduction due to SOC is merely 0.01 eV, but the band-edge values of σ^{yyy} and σ^{yxx} computed with SOC reduce to 450 and 2200 μA/V^2 from their PBE values of 1000 and 3000 μA/V^2, respectively; the PBE and PBE + SOC spectra are almost identical for higher photon frequencies. Interestingly, compared to the HSE values of 150 and 250 μA/V^2, the peak values of σ^{yyy} and σ^{yxx} estimated with HSE + SOC increase to 300 and 400 μA/V^2, respectively. In addition, the HSE and HSE + SOC spectrum profiles are notably different for both σ^{yyy} and σ^{yxx} in the frequency range between 1.5 and 3.0 eV.

To get a better understanding of the subtle changes in the shift current responses due to SOC, we analyze the spectrum of σ^{yyy} by plotting two BZ-integrated quantities: the energy averaged shift vector $\overline{R}^{a,b}$ and the transition intensity ε_2^{bb} defined as

$$\overline{R}^{a,b}(\omega) = \sum_k \sum_{nm} f_{nm} R^{a,b}_{nm} \delta(\omega_{mn} - \omega) \quad (1)$$

and

$$\varepsilon_2^{bb}(\omega) = \sum_k \sum_{nm} r^b_{nm} r^b_{mn} \delta(\omega_{mn} - \omega), \quad (2)$$

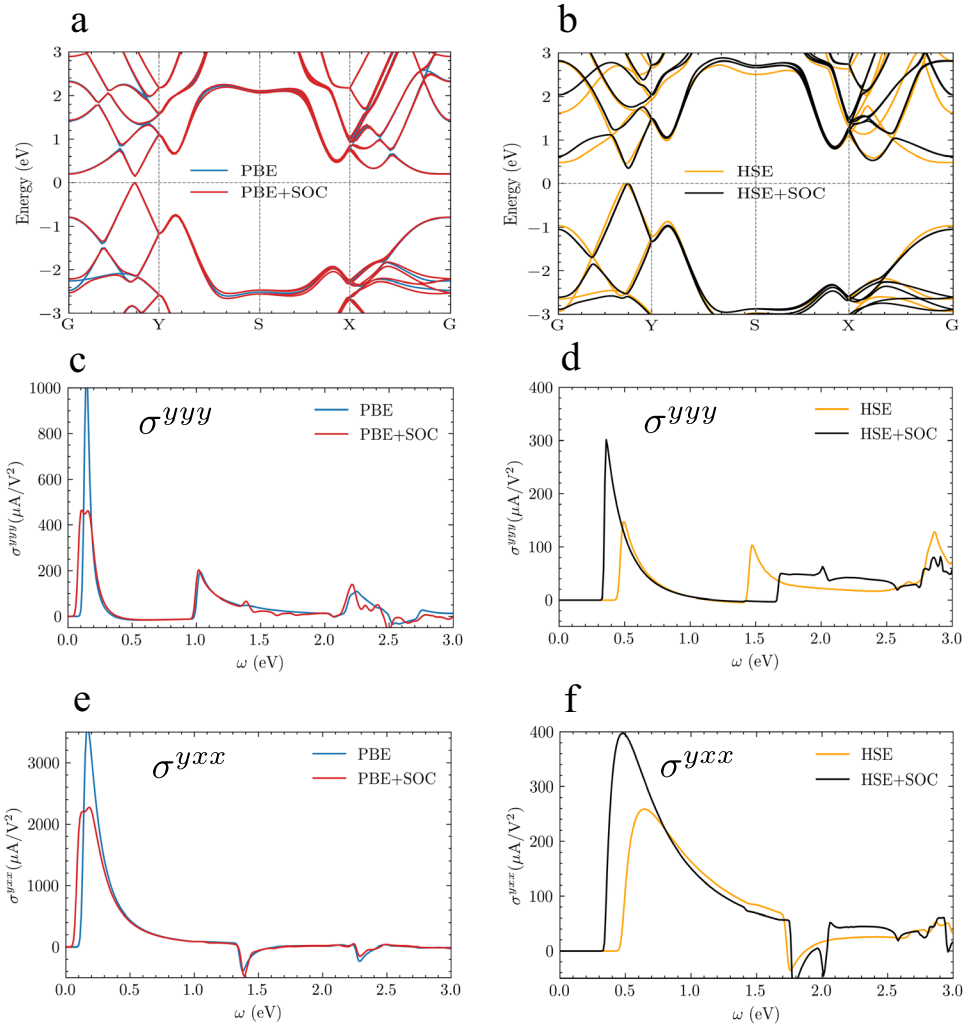

Fig. 2 Electronic band structures and shift current spectra of monolayer As. Band structures computed with **a** PBE and PBE+SOC and **b** HSE and HSE+SOC. σ^{yyy} spectra computed with **c** PBE and PBE+SOC and **d** HSE and HSE+SOC. σ^{yxx} spectra computed with **e** PBE and PBE+SOC and **f** HSE and HSE+SOC.

respectively. For a given photon frequency ω, $\overline{R}^{a,b}(\omega)$ is a measure of aggregate contributions of shift vectors $R^{a,b}_{nm}$ at all k points in the BZ; $\varepsilon_2^{bb}(\omega)$ reflects the photon absorption strength. By comparing the spectra of $\overline{R}^{y,y}$ and ε_2^{yy} computed with PBE, PBE + SOC, HSE, and HSE + SOC (Fig. 3), we find that the integrated shift vectors are comparable at the low-frequency region but these four methods predict rather different transition intensities near the band edge. Specifically, PBE predicts a larger magnitude of ε_2^{yy} than PBE + SOC, whereas HSE yields a lower transition intensity than HSE+SOC. Therefore, the SOC effect suppresses the transition at the PBE level but promotes the transition in HSE. According to eq. (2), the magnitude of ε_2^{yy} depends on the interband Berry connections between every conduction and valence band pair that has the energy difference matching the energy of the incident light. The presence of SOC, regardless the strength, will lift the spin degeneracy and lead to level anticrossing at some k points. These changes in electronic bands albeit localized in the momentum space could strongly affect the interband Berry connections. Therefore, the pronounced SOC effect on the spectrum of ε_2 and then σ is a manifestation of the topological nature of shift current that exhibits highly nontrivial dependence on the Berry connections of a bundle of Bloch bands (valence and conduction bands relevant to photon excitation).

Previous studies have demonstrated that the shift current response of 2D materials can exist a significant dependence on the layer number[15,53,54]. We examine the layer stacking impact on the response functions. Our HSE+SOC calculations indicate that bilayer As remains polar and possesses a small band gap of 0.36 eV (Fig. 4a), whereas trilayer As becomes centrosymmetric and metallic. The shift current spectrum is presented in Fig. 4b, revealing a peak value of 125 $\mu A/V^2$ for σ^{yyy} and -135 $\mu A/V^2$ for σ^{yxx}; these magnitudes are smaller than those in monolayer, consistent with those observed experimentally in $CuInP_2S_6$ where the photocurrent density decreases drastically when the thickness exceeds ≈40 nm[15].

We believe HSE+SOC is the most reliable method among the ones employed in the current work and most previous works, and the predicted peak shift current response in monolayer As is 400 $\mu A/V^2$ for σ^{yxx}, much higher than previous reports for 2D materials, i.e., 100 $\mu A/V^2$ in GeS. This highlights the potential of elemental ferroelectric 2D materials for photoelectric conversion.

Monolayer antimony

The band structures and shift current spectra of monolayer Sb computed with four different methods are displayed in Fig. 5. The direct band gap values based on the band structures plotted

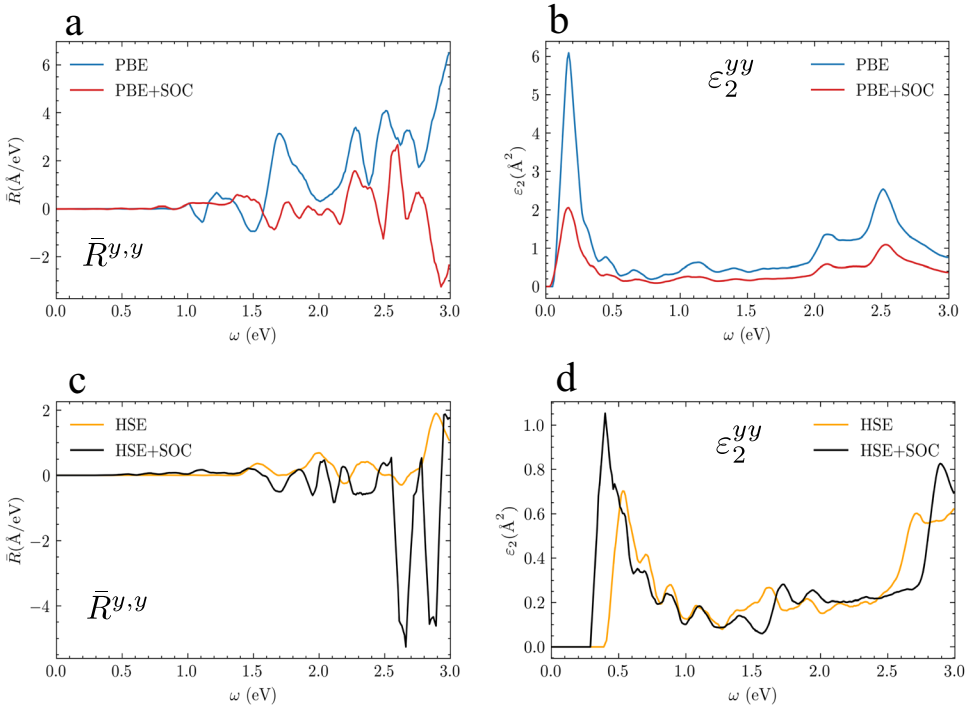

Fig. 3 Shift vector and transition intensity in monolayer As. BZ-integrated shift vector ($\bar{R}^{y,y}$) and transition intensity (ε_2^{yy}) for σ^{yyy} in monolayer As. $\bar{R}^{y,y}$ estimated with **a** PBE and PBE+SOC and **c** HSE and HSE+SOC. ε_2^{yy} estimated with **b** PBE and PBE+SOC and **d** HSE and HSE +SOC.

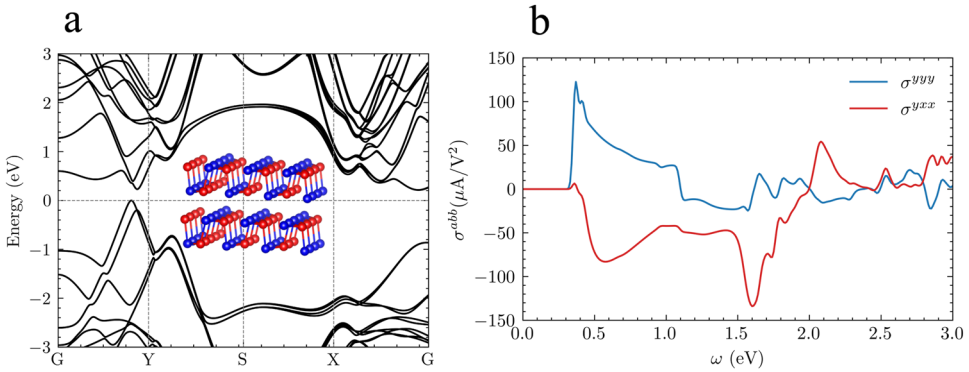

Fig. 4 Band structure and shift current in bilayer As. a Electronic band structure and **b** shift current σ^{yyy} and σ^{yxx} spectra for bilayer As calculated with HSE+SOC. The inset in **a** shows the structure of bilayer As.

along high-symmetry lines are 0.31, 0.32, 0.41, and 0.29 eV for PBE, PBE+SOC, HSE, and HSE + SOC, respectively. Despite yielding comparable band structures, these four methods predict distinct shift current spectra. Similar to the case of monolayer As, we observe a reduction of band-edge response magnitude of σ^{yyy} (σ^{yxx}) from −1000 (4000) μA/V^2 in PBE (Fig. 5c, e) to −300 (1700) μA/V^2 in HSE (Fig. 5d, f), reaffirming the importance of including exact exchange in DFT calculations.

The inclusion of the SOC effect completely changes the spectrum profiles of σ^{yyy} and σ^{yxx} at the PBE level (Fig. 5c, e). The most striking result is the reversal of the current direction for low-frequency excitations. For example, PBE predicts a current running against the polarization ($\sigma^{yyy} < 0$) but PBE+SOC predicts a current flowing along the polarization ($\sigma^{yyy} > 0$). The sign of the shift current is determined by the integrated shift vector as defined in eq. (1). Indeed, as shown in Fig. 6a, the sign of $\bar{R}^{y,y}$ is the same as the sign of σ^{yyy}, and SOC causes a sign change. For a given photon energy ω, the value of $\bar{R}^{a,b}$ depends on the topological quantity $R_{nm}^{a,b}$ at every k point in the BZ that supports resonant excitation. Following our previous argument regarding the effect of SOC on the transition intensity, the intraband Berry connection ($\mathcal{A}$) of some bands may be altered drastically by SOC, particularly around the k point where SOC induces a hybridization gap. Therefore, it is physically plausible to have a sign-changing situation due to SOC, as demonstrated in the case of monolayer Sb when treated with PBE. We further compute k-resolved $\bar{R}^{y,y}$ at a photon energy of 0.2 eV with PBE and PBE+SOC, respectively, with results ploted in Fig. 6e and f. It is found that all k-resolved $\bar{R}^{y,y}$ computed with PBE have negative values whereas those computed with PBE+SOC become mostly positive.

At the HSE level, SOC causes a redshift of the band-edge peak to ≈0.1 eV for both σ^{yyy} and σ^{yxx} (Fig. 5d, f), though the band gap value taken from the HSE+SOC band structures is 0.29 eV, higher than the onset photon energy. We further decompose σ^{yyy} into $\bar{R}^{y,y}$ and ε_2^{yy} and find that the magnitudes of $\bar{R}^{y,y}$ computed with HSE and HSE+SOC are comparable at the low-frequency region

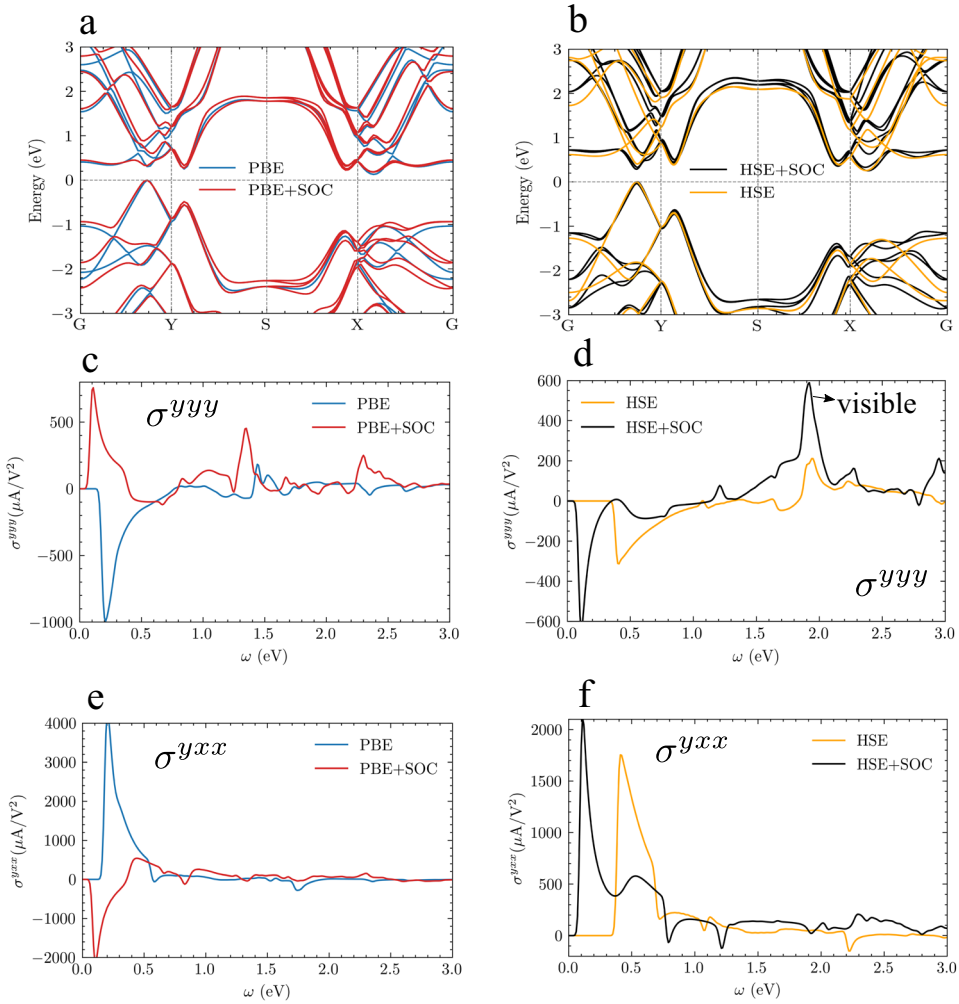

Fig. 5 Electronic band structures and shift current spectra of monolayer Sb. Band structures computed with **a** PBE and PBE+SOC and **b** HSE and HSE+SOC. σ^{yyy} spectra computed with **c** PBE and PBE+SOC and **d** HSE and HSE+SOC. σ^{yxx} spectra computed with **e** PBE and PBE+SOC and **f** HSE and HSE+SOC.

(Fig. 6c). However, the ε_2^{yy} spectrum of HSE+SOC has a sharp peak at a much lower frequency of 0.1 eV (Fig. 6d), consistent with the HSE+SOC spectrum of σ^{yyy} (Fig. 5d). This seems to suggest forbidden optical excitations with in-gap photon frequencies. To resolve this puzzle, we perform a diagnostic analysis on the electronic structures of monolayer Sb obtained with HSE and HSE +SOC. The zoomed-in band structures along Γ-Y-S presented in Fig. 7a show that the inclusion of SOC gives a smaller band gap of 0.29 eV than the HSE band gap of 0.4 eV, and breaks the spin degeneracy. We compute the JDOS defined as

$$\rho(\omega) = \int \frac{d\boldsymbol{k}}{8\pi^3}\delta(\omega_{nm} - \omega) \tag{3}$$

with results plotted in Fig. 7b. The onset frequency of the HSE JDOS is 0.4 eV, as expected from the HSE band gap. However, the JDOS computed with HSE+SOC acquires nonzero values staring at a lower frequency of 0.1 eV. As the JDOS is obtained by integrating over the whole BZ while the band structure only shows the band energies along the high-symmetry BZ boundary paths, the JDOS of HSE + SOC hints at a smaller gap at a generic *k*-point. We thus map out the energy difference between the highest valence band and the lowest conduction band over the whole BZ (Fig. 7c, d) with HSE and HSE+SOC, respectively. Indeed, HSE gives a gap of 0.38 eV at a *k* point very close to the high-symmetry line Γ-Y (Fig. 7c); HSE+SOC yields a band gap of 0.1 eV at a generic *k*-point ([0.04, 0.35] in reduced coordinates) away from the zone boundary (Fig. 7d), consistent with the onset photon frequency for σ^{yyy} and σ^{yxx} predicted by HSE+SOC (Fig. 5d, f). It is noted that the peak value of σ^{yxx} in monolayer Sb estimated with HSE+SOC reaches 2000 $\mu A/V^2$, even higher than monolayer As. Moreover, the value of σ^{yyy} reaches 600 $\mu A/V^2$ at $\omega = 1.8$ eV, suitable for visible light absorption.

It is noted that we have compared the shift current spectrum and JDOS of monolayer GeS, a model material for investigating BPVE in 2D, with monolayer Sb. The peak shift current in GeS is ≈100 $\mu A/V^2$, one order of magnitude smaller than that in monolayer Sb. We find that monolayer Sb exhibits much larger JDOS than GeS. Nevertheless, because GeS has a much larger band gap than Sb and the shift current scales inversely with the band gap according to velocity gauge formalism[17], we suggest that the giant shift current in monolayer Sb could be attributed to multiple factors including small band gap and large JDOS.

Monolayer bismuth

Since Bi has a larger atomic number, the SOC effect is more pronounced in monolayer Bi as demonstrated from the notably different band structures between PBE (HSE) and PBE + SOC (HSE + SOC), as shown in Fig. 8a, b. Without SOC, PBE and HSE predict similar spectrum profiles of σ^{yyy} and σ^{yxx} and large band-edge

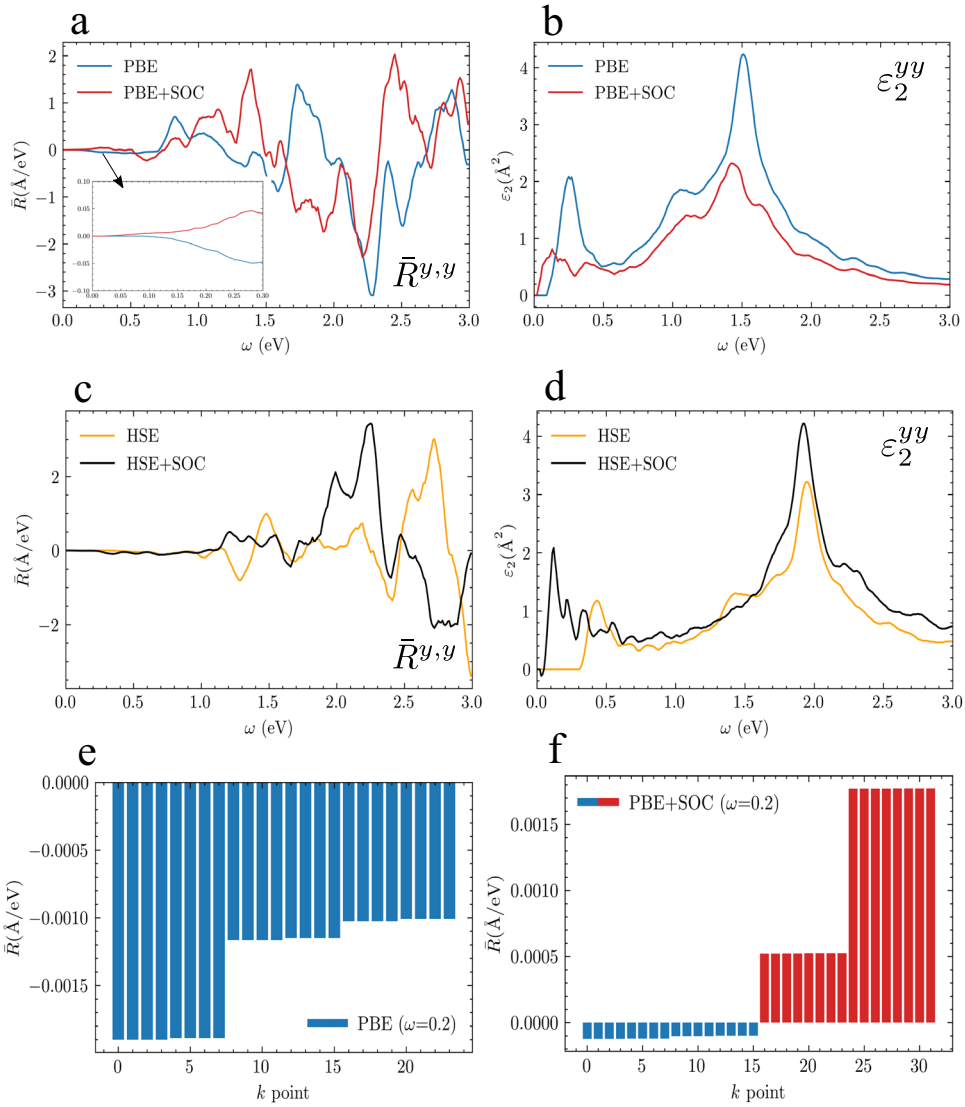

Fig. 6 Shift vector and transition intensity in monolayer Sb. BZ-integrated shift vector ($\bar{R}^{y,y}$) and transition intensity (ε_2^{yy}) for σ^{yyy} in monolayer Sb. $\bar{R}^{y,y}$ estimated with **a** PBE and PBE+SOC and **c** HSE and HSE+SOC. ε_2^{yy} estimated with **b** PBE and PBE+SOC and **d** HSE and HSE+SOC. **e**, **f** *k*-reolsved shift vector calculate at $\omega = 0.2$ for PBE and PBE+SOC.

responses. The magnitude of the peak response of σ^{yxx} computed with HSE is close to 6500 μA/V^2. In comparison, the spectra obtained with SOC are qualitatively different. In general, the spectra of PBE+SOC and HSE+SOC share similar peak structures with the latter predicting lower peak values (Fig. 8c–f). For example, PBE+SOC predicts a main peak of -2000 μA/V^2 at 1.0 eV for σ^{yyy} while the HSE + SOC spectrum of σ^{yyy} has the highest peak of -500 μA/V^2 located at 1.4 eV. We note that the band-edge response is no longer the strongest. The spectrum of ε_2^{yy} (Fig. 9b) confirms that the SOC interaction reduces the band-edge photon absorption than that in HSE. Given the substantially different band structures predicted by HSE and HSE+SOC, it is not surprising to obtain drastically different spectra of $\bar{R}^{y,y}$ (Fig. 9a). For monolayer Bi, the inclusion of SOC is crucial to acquire correct shift current spectrum.

Strain effect

Because reduced-dimensional structures can sustain much larger strains than their bulk counterparts, it has become common to use strain to modulate the structural, electronic, and optical properties of 2D materials[55–58]. Here, we explore the effect of uniaxial strain (η_x) on the shift current response. Taking monolayer As for example, we find that a tensile strain along the *x* direction can effectively reduce the band gap and promote the current density. As shown in Fig. 10, a 3% tensile strain enhances both σ^{yyy} and σ^{yxx} by nearly fourfold. In contrast, a compressive strain ($\eta_x = -3$ %) increases the band gap hence reduces the band-edge response. Interestingly, the peak of σ^{yyy} at a higher photon energy of 1.6 eV gets enhanced by the compressive strain of -3%. Similar tensile strain-promoted response is also found in monolayer Sb. In particular, the magnitude of σ^{yxx} gets enhanced to 2800 μA/V^2 when stretching the monolayer by 2% along *x* (Fig. 10d).

Finally, we compare the shift current responses of different materials including bulk polar materials (e.g., $PbTiO_3$, $BaTiO_3$, and GaAs) and 2D materials (e.g., GeSe and CrI_3). As summarized in Fig. 11a, the magnitude of the response tensor roughly scales inversely with the band gap, and the stretched monolayer Sb has the highest response of 2800 μA/V^2. Note that most previous results were based on PBE calculations, which generally overestimate the response. To compare with experimental data, we further estimate the shift photocurrent density based on the

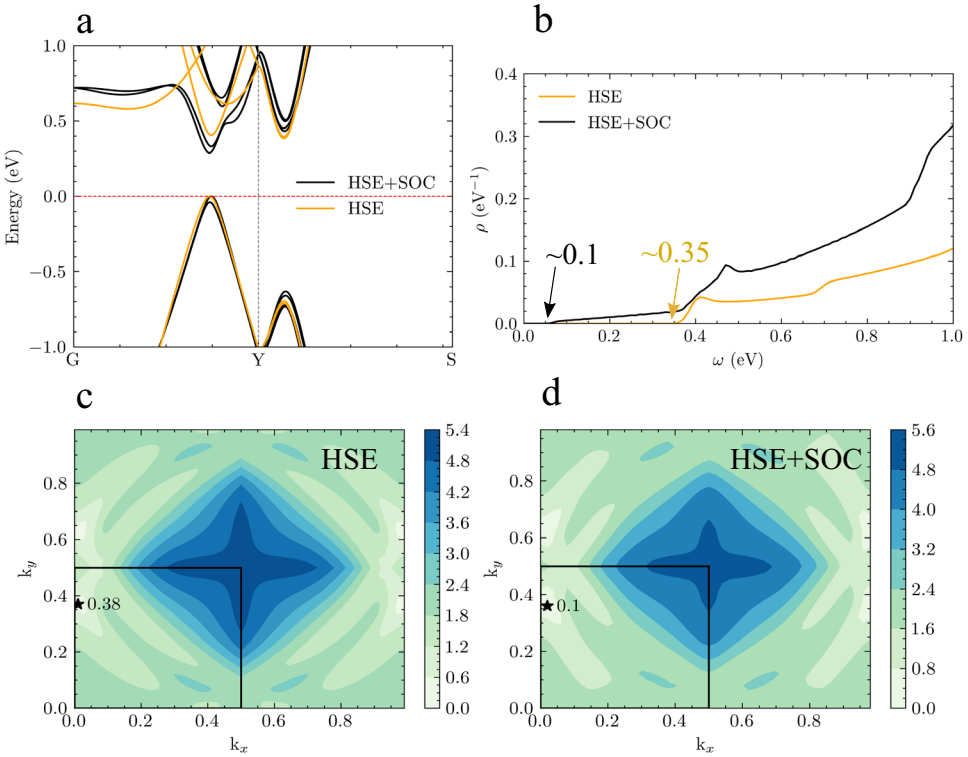

Fig. 7 Analysis of the electronic structure of monolayer Sb. a Zoomed-in band structures calculated with HSE and HSE+SOC. **b** Joint density of states. Contour plots of the energy difference between the highest valence band and the lowest conduction band over the whole 2D BZ obtained with **c** HSE and **d** HSE+SOC. The star symbol labels the direct band gap.

computed response tensor and a light intensity of 0.1 W/cm^2 following the method in ref. [33]. It is evident from Fig. 11b that elemental 2D ferroelectrics represented by Sb, As, and Bi outperform conventional bulk ferroelectrics and 2D layered materials such as $CuInP_2S_6$ over a wide range of wavelengths including the visible light spectrum. It is worth noting that TaAs exhibits a strong response at a wavelength of ≈10,000 nm, which is much larger than the wavelengths of visible light. Given TaAs is a Weyl semimetal, it is not surprising that its shift current response is large because of the gapless band dispersion and topological nature. The mid-infrared response is likely more relevant to applications such as optical detectors and sensors. In comparison, monolayers As and Sb exhibit large shift current response across a wide range of wavelengths including the visible light spectrum, which would be advantageous for utilizing most of the solar spectrum. Additionally, since the peak responses of group-V elemental ferroelectrics are consistent with light-induced terahertz emission, the large current magnitude suggests their potential applications in terahertz source platforms.

In this work, we investigate the shift current responses in single-element two-dimensional ferroelectrics represented by monolayer As, Sb, and Bi in the space group of $Pmn2_1$ using first-principles density functional theory calculations. We find that PBE and HSE yield qualitatively different shift current spectra, demonstrating the importance of exact exchange potential for reliable predictions of optical responses. Moreover, the spin-orbit coupling, largely overlooked in previous studies, can substantially affect the magnitude, sign, and spectral profile of shift current even for light elements such as arsenic. This highlights the topological nature of shift current that has nontrivial dependence on both intraband and interband Berry connections of a bundle of valence and conduction bands. Regarding computational materials by design for new solar materials that can generate large shift currents, we suggest that it is essential to treat the electronic exchange–correlation interaction beyond the generalized gradient approximation and to include the spin-orbit interaction in density functional theory calculations. Based on the results predicted by HSE+SOC, we propose that elemental 2D ferroelectrics can support large shift currents, outperforming many state-of-the-art materials. This work unravels the potential of elemental 2D ferroelectrics for photovolatic and optoelectronic applications.

METHOD

We follow the formalism adopted in Refs. [59,60] to compute the photon frequency-dependent shift current spectrum. The shift current density (J_2) is regarded as a second-order optical response to the electromagnetic field E of frequency ω,

$$J_2^a = 2\sum_{bc}\sigma^{abc}(0;\omega,-\omega)E^b(\omega)E^c(-\omega), \tag{4}$$

where the third-rank tensor $\sigma^{abc}(0;\omega,-\omega)$ is the shift current response tensor; a, b, and c are Cartesian indexes, and the index a specifies the direction of the generated DC current, while b and c are polarization directions of an incident light. Within the length gauge, the shift current tensor is derived as

$$\sigma^{abc}(0;\omega,-\omega) = -\frac{i\pi e^3}{2\hbar^2}\int\frac{d\boldsymbol{k}}{8\pi^3}\sum_{nm} f_{nm}(r^b_{mn}r^c_{nm;a} + r^c_{mn}r^b_{nm;a})\delta(\omega_{mn}-\omega), \tag{5}$$

where n and m are band indexes, and $\boldsymbol{k}$ is the wavevector of the Bloch wave function. $f_{nm} = f_n - f_m$ is the difference in the Fermi-Dirac occupation number between bands n and m; $\omega_{nm} = \omega_n - \omega_m$ represents the band energy difference. $r^b_{nm} = i\langle n|\partial k^b|m\rangle$ is the dipole matrix element (interband Berry connection). $r^b_{nm;a}$ is the generalized derivative expressed as $r^b_{nm;a} = \frac{\partial r^b_{nm}}{\partial k^a} - ir^b_{nm}(\mathcal{A}^a_n - \mathcal{A}^a_m)$ with $\mathcal{A}^a_n = i\langle n|\partial k^a|n\rangle$ the intraband Berry connection.

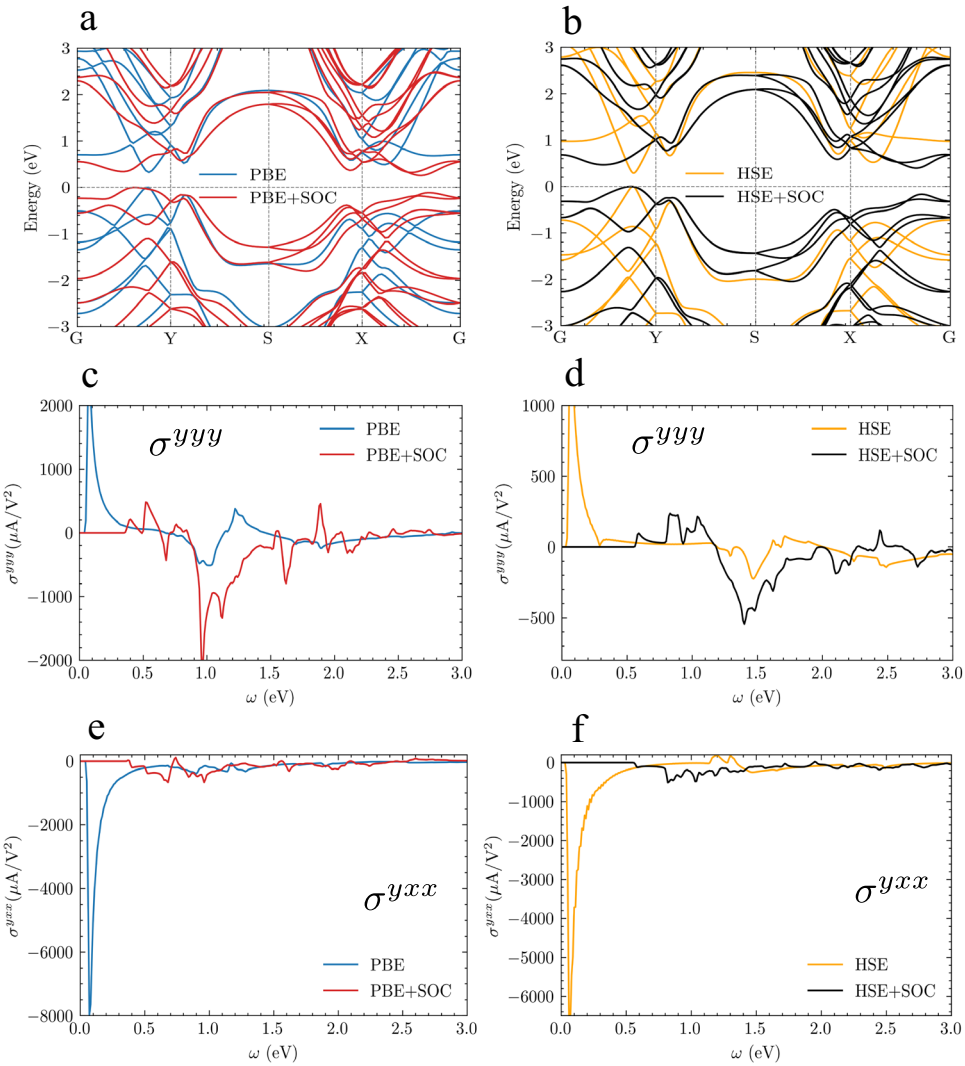

Fig. 8 Electronic band structures and shift current spectra of monolayer Bi. Band structures computed with **a** PBE and PBE+SOC and **b** HSE and HSE+SOC. σ^{yyy} spectra computed with **c** PBE and PBE+SOC and **d** HSE and HSE+SOC. σ^{yxx} spectra computed with **e** PBE and PBE+SOC and **f** HSE and HSE+SOC.

Under a linearly polarized light ($b = c$), the shift current response tensor can be re-formulated into a more compact expression,

$$\sigma^{abb}(0;\omega,-\omega) = \frac{\pi e^3}{\hbar^2}\int \frac{d\boldsymbol{k}}{8\pi^3}\sum_{nm} f_{nm} R^{a,b}_{nm} r^b_{nm} r^b_{mn} \delta(\omega_{mn} - \omega), \qquad (6)$$

where $R^{a,b}_{nm} = \frac{\partial \phi^b_{nm}}{\partial k^a} + \mathcal{A}^a_n - \mathcal{A}^a_m$ is the shift vector with ϕ_{nm} being the phase factor of the dipole matrix element $r^b_{nm} = |r^b_{nm}|e^{-i\phi^b_{nm}}$. The shift vector has a unit of length and represents the average displacement of the coherent photoexcited carriers during their lifetimes. The $r^b_{nm} r^b_{mn}$ term measures the transition intensity which describes the optical absorption strength for the transition from band m to band n. Therefore, the response tensor can be viewed as the product of shift-vector and optical transition intensity.

The structural parameters of monolayer As, Sb, and Bi are optimized using `Quantum Espresso`[61,62] with Garrity–Bennett–Rabe–Vanderbilt (GBRV) ultrasoft pseudopotentials[63]. The exchange-correlation functional is treated within the generalized gradient approximation of Perdew–Burke–Ernzerhof (PBE) type[64]. We use a plane-wave kinetic energy cutoff of 50 Ry, a charge density cutoff of 250 Ry, a $12 \times 12 \times 1$ Monkhorst-Pack k-point mesh for Brillouin zone (BZ) integration, an ionic energy convergence threshold of 10^{-5} Ry, and a force convergence threshold of 10^{-4} Ry in structural optimizations. Maximally localized Wannier functions to fit DFT electronic structures are obtained using the `Wannier90` code[65], and then the shift current response tensor is calculated in the Wannier basis as described in ref. [59]. We use a numerical smearing parameter of 20 meV and a dense k-point grid of $1000 \times 1000 \times 1$ to ensure the spectrum convergence. In addition, the 3D-like response is estimated by rescaling the calculated 2D response with the effective thickness of monolayer[33]. The spin-orbit coupling (SOC) is taken into account at the fully relativistic level with norm-conserving pseudopotentials provided by the PseudoDoJo project[66]. We also compute the shift current using the Heyd-Scuseria-Ernzerhof (HSE) hybrid functional[67] with a $8 \times 8 \times 1q$-point grid during the self-consistent-field cycles. The HSE band structure is obtained via Wannier interpolation[68] using `Wannier90` interfaced with `Quantum Espresso`. We employ the `Wannier Berri` code[69,70] to compute the shift vector and transition intensity (see discussions below) to analyze the shift current spectrum. It is noted that all shift current calculations are based on the independent-particle approximation and do not take the exciton effect into account.

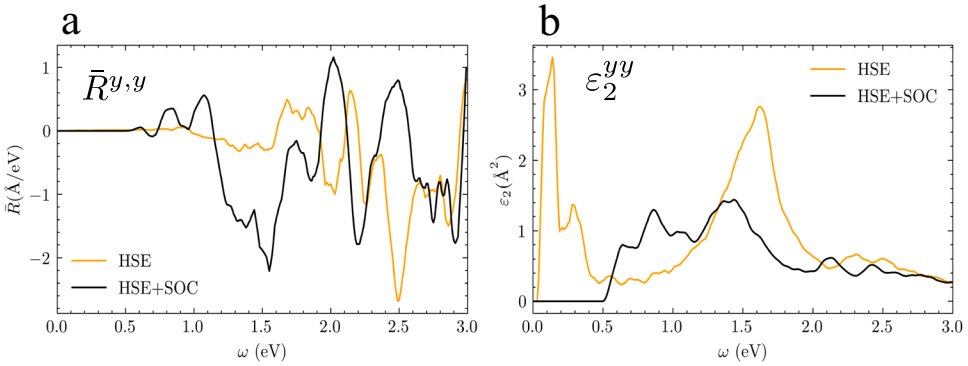

Fig. 9 Shift vector and transition intensity in monolayer Bi. BZ-integrated **a** shift vector and **b** transition intensity for σ^{yyy} in monolayer Bi computed with HSE and HSE+SOC.

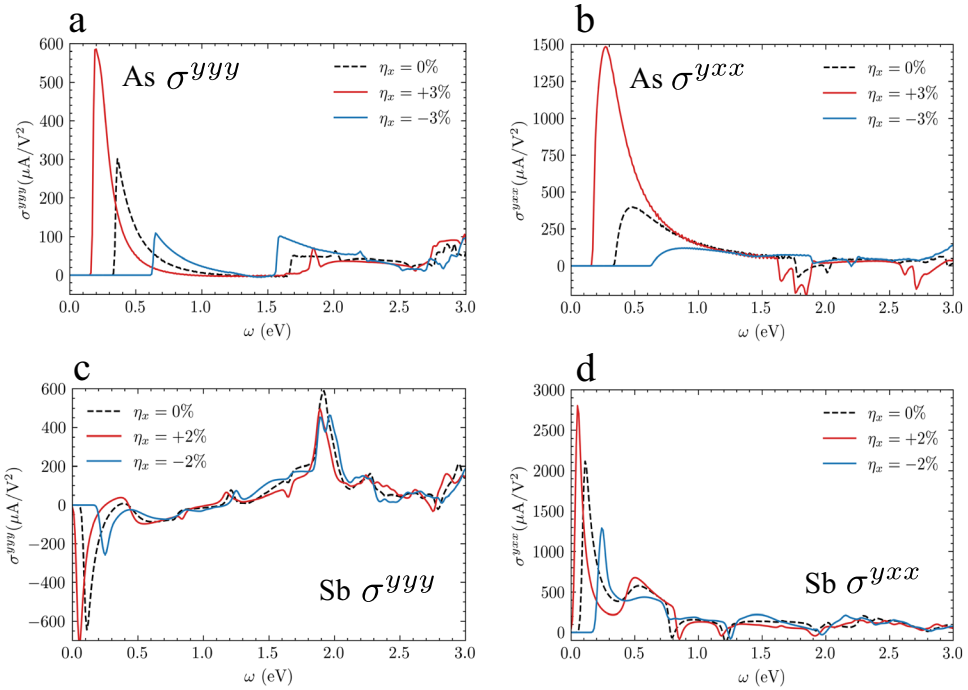

Fig. 10 Uniaxial strain tuning of shift current. Uniaxial strain dependence of **a**, **c** σ^{yyy} and **b**, **d** σ^{yxx} of monolayer As and Sb.

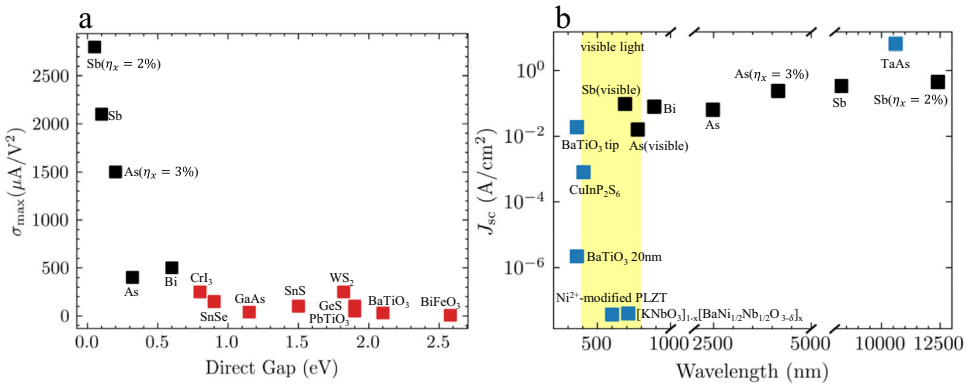

Fig. 11 Comparison of shift current response and current density of different materials. a Peak value of shift current response[29,33,36,59,60] and **b** current density[4,7,8,10–12,15] of different materials assuming a light intensity of 0.1 W/cm^2. Besides strong band-edge responses to long-wavelength light, monolayer Sb and As can generate large shift currents in response to visible light illumination.

DATA AVAILABILITY

The data that support the findings of this study are included in this article and are available from the corresponding author upon reasonable request.

Received: 30 November 2022; Accepted: 15 April 2023;
Published online: 27 April 2023

REFERENCES

1. Shockley, W. & Queisser, H. J. Detailed balance limit of efficiency of $p-n$ junction solar cells. *J. Appl. Phys.* **32**, 510 (1961).
2. B. I., Sturman and V. M., Fridkin, *The Photovoltaic and Photorefractive Effects in Noncentrosymmetric Materials* (Routledge, 2021)
3. Fridkin, V. M. Bulk photovoltaic effect in noncentrosymmetric crystals. *Crystallogr. Rep.* **46**, 654 (2001).
4. Grinberg, I. et al. Perovskites oxides for visible-light-adsorbing ferroelectric and photovoltaic materials. *Naure* **503**, 509 (2013).
5. Butler, K. T., Frost, J. M. & Walsh, A. Ferroelectric materials for solar energy conversion: photoferroics revisited. *Energy Environ. Sci.* **8**, 838 (2015).
6. Tan, L. Z. et al. Shift current bulk photovoltaic effect in polar materials—hybrid and oxide perovskites and beyond. *npj Comput. Mater.* **2**, 16026 (2016).
7. Spanier, J. E. et al. Power conversion efficiency exceeding the shockley–queisser limit in a ferroelectric insulator. *Nat. Photonics* **10**, 611 (2016).
8. Zenkevich, A. et al. Giant bulk photovoltaic effect in thin ferroelectric $BaTiO_3$ films. *Phys. Rev. B* **90**, 161409 (2014).
9. Nakamura, M. et al. Shift current photovoltaic effect in a ferroelectric charge-transfer complex. *Nat. Commun.* **8**, 281 (2017).
10. Pal, S. et al. Giant photovoltaic response in band engineered ferroelectric perovskite. *Sci. Rep.* **8**, 8005 (2018).
11. Osterhoudt, G. B. et al. Colossal mid-infrared bulk photovoltaic effect in a type-i weyl semimetal. *Nat. Mater.* **18**, 471 (2019).
12. Huangfu, G. et al. Visible or near-infrared light self-powered photodetectors based on transparent ferroelectric ceramics. *ACS Appl. Mater. Interfaces* **12**, 33950 (2020).
13. Zhang, Y. J. et al. Enhanced intrinsic photovoltaic effect in tungsten disulfide nanotubes. *Nature* **570**, 349 (2019).
14. Yang, S. Y. et al. Above-bandgap voltages from ferroelectric photovoltaic devices. *Nat. Nanotechnol.* **5**, 143 (2010).
15. Li, Y. et al. Enhanced bulk photovoltaic effect in two-dimensional ferroelectric $CuInP_2S_6$. *Nat. Commun.* **12**, 5896 (2021).
16. Burger, A. M. et al. Direct observation of shift and ballistic photovoltaic currents. *Sci. Adv.* **5**, eaau5588 (2019).
17. Kraut, W. & von Baltz, R. Anomalous bulk photovoltaic effect in ferroelectrics: A quadratic response theory. *Phys. Rev. B* **19**, 1548 (1979).
18. von Baltz, R. & Kraut, W. Theory of the bulk photovoltaic effect in pure crystals. *Phys. Rev. B* **23**, 5590 (1981).
19. Aversa, C. & Sipe, J. E. Nonlinear optical susceptibilities of semiconductors: Results with a length-gauge analysis. *Phys. Rev. B* **52**, 14636 (1995).
20. Sipe, J. E. & Shkrebtii, A. I. Second-order optical response in semiconductors. *Phys. Rev. B* **61**, 5337 (2000).
21. Fregoso, B. M. Bulk photovoltaic effects in the presence of a static electric field. *Phys. Rev. B* **100**, 064301 (2019).
22. Sturman, B. I. Ballistic and shift currents in the bulk photovoltaic effect theory. *Phys.–Usp.* **63**, 407 (2020).
23. Panday, S. R., Barraza-Lopez, S., Rangel, T. & Fregoso, B. M. Injection current in ferroelectric group-IV monochalcogenide monolayers. *Phys. Rev. B* **100**, 195305 (2019).
24. Dai, Z., Schankler, A. M., Gao, L., Tan, L. Z. & Rappe, A. M. Phonon-assisted ballistic current from first-principles calculations. *Phys. Rev. Lett.* **126**, 177403 (2021).
25. Glass, A. M., von der Linde, D. & Negran, T. J. High-voltage bulk photovoltaic effect and the photorefractive process in $LiNbO_3$. *Appl. Phys. Lett.* **25**, 233 (1974).
26. Barik, T. & Sau, J. D. Nonequilibrium nature of nonlinear optical response: Application to the bulk photovoltaic effect. *Phys. Rev. B* **101**, 045201 (2020).
27. Ahn, J., Guo, G.-Y. & Nagaosa, N. Low-frequency divergence and quantum geometry of the bulk photovoltaic effect in topological semimetals. *Phys. Rev. X* **10**, 041041 (2020).
28. Nastos, F. & Sipe, J. E. Optical rectification and shift currents in GaAs and GaP response: Below and above the band gap. *Phys. Rev. B* **74**, 035201 (2006).
29. Young, S. M. & Rappe, A. M. First principles calculation of the shift current photovoltaic effect in ferroelectrics. *Phys. Rev. Lett.* **109**, 116601 (2012).
30. Young, S. M., Zheng, F. & Rappe, A. M. First-principles calculation of the bulk photovoltaic effect in bismuth ferrite. *Phys. Rev. Lett.* **109**, 236601 (2012).
31. Young, S. M., Zheng, F. & Rappe, A. M. First-principles materials design of high-performing bulk photovoltaics with the $LiNbO_3$ structure. *Phys. Rev. Appl.* **4**, 054004 (2015).
32. Tan, L. Z. & Rappe, A. M. Upper limit on shift current generation in extended systems. *Phys. Rev. B* **100**, 085102 (2019).
33. Rangel, T. et al. Large bulk photovoltaic effect and spontaneous polarization of single-layer monochalcogenides. *Phys. Rev. Lett.* **119**, 067402 (2017).
34. Wang, H. & Qian, X. Ferroicity-driven nonlinear photocurrent switching in time-reversal invariant ferroic materials. *Sci. Adv.* **5**, eaav9743 (2019).
35. Tiwari, R. P. Enhanced shift current bulk photovoltaic effect in ferroelectric rashba semiconductor α-GeTe: ab initio study from three- to two-dimensional van der waals layered structures. *J. Phys. Condens. Matter* **34**, 435404 (2022).
36. Zhang, Y. et al. Switchable magnetic bulk photovoltaic effect in the two-dimensional magnet CrI_3. *Nat. Commun.* **10**, 3783 (2019).
37. Xu, H., Wang, H., Zhou, J. & Li, J. Pure spin photocurrent in non-centrosymmetric crystals: bulk spin photovoltaic effect. *Nat. Commun.* **12**, 4330 (2021).
38. Xiao, R. C. et al. Non-synchronous bulk photovoltaic effect in two-dimensional interlayer-sliding ferroelectrics. *npj Comput. Mater.* **8**, 138 (2022).
39. Kim, B., Park, N. & Kim, J. Giant bulk photovoltaic effect driven by the wall-to-wall charge shift in WS_2 nanotubes. *Nat. Commun.* **13**, 3237 (2022).
40. Liu, S., Zheng, F. & Rappe, A. M. Giant bulk photovoltaic effect in vinylene-linked hybrid heterocyclic polymer. *J. Phys. Chem. C* **121**, 6500 (2017).
41. Tan, L. Z. & Rappe, A. M. Enhancement of the bulk photovoltaic effect in topological insulators. *Phys. Rev. Lett.* **116**, 237402 (2016).
42. Xu, H. et al. Colossal switchable photocurrents in topological janus transition metal dichalcogenides. *npj Comput. Mater.* **7**, 31 (2021).
43. Xu, H., Wang, H. & Li, J. Abnormal nonlinear optical responses on the surface of topological materials. *npj Comput. Mater.* **8**, 111 (2022).
44. Xu, H., Zhou, J. & Li, J. Light-induced quantum anomalous hall effect on the 2D surfaces of 3D topological insulators. *Adv. Sci.* **8**, 2101508 (2021).
45. Ji, Z. et al. Spatially dispersive circular photogalvanic effect in a weyl semimetal. *Nat. Mater.* **18**, 955 (2019).
46. Cook, A. M., Fregoso, B. M., de Juan, F., Coh, S. & Moore, J. E. Design principles for shift current photovoltaics. *Nat. Commun.* **8**, 14176 (2017).
47. Xiao, C. et al. Elemental ferroelectricity and antiferroelectricity in group-V monolayer. *Adv. Funct. Mater.* **28**, 1707383 (2018).
48. Xu, F. et al. Controllable ferroelectricity and bulk photovoltaic effect in elemental group-v monolayers through strain engineering. *Phys. Rev. B* **106**, 195418 (2022).
49. Wan, W., Liu, C., Xiao, W. & Yao, Y. Promising ferroelectricity in 2d group IV tellurides: a first-principles study. *Appl. Phys. Lett.* **111**, 132904 (2017).
50. Wang, X. S., Kushvaha, S. S., Yan, Z. & Xiao, W. Self-assembly of antimony nanowires on graphite. *Appl. Phys. Lett.* **88**, 233105 (2006).
51. Bianchi, M. et al. Surface states on a topologically nontrivial semimetal: The case of Sb(110). *Phys. Rev. B* **85**, 155431 (2012).
52. Nagao, T. et al. Nanofilm allotrope and phase transformation of ultrathin bi film on Si(111)-7 × 7. *Phys. Rev. Lett.* **93**, 105501 (2004).
53. Strasser, A., Wang, H. & Qian, X. Nonlinear optical and photocurrent responses in janus MoSSe monolayer and MoS_2-MoSSe van der waals heterostructure. *Nano Lett.* **22**, 4145 (2022).
54. Mu, X., Xue, Q., Sun, Y. & Zhou, J. Magnetic proximity enabled bulk photovoltaic effects in van der waals heterostructures. *Phys. Rev. Res.* **5**, 013001 (2023).
55. Xu, R. et al. Strain-induced room-temperature ferroelectricity in $SrTiO_3$ membranes. *Nat. Commun.* **11**, 3141 (2020).
56. Li, Z. et al. Efficient strain modulation of 2D materials via polymer encapsulation. *Nat. Commun.* **11**, 1151 (2020).
57. Zhao, C. et al. Strain tunable semimetal–topological-insulator transition in monolayer 1-T′-WTe_2. *Phys. Rev. Lett.* **125**, 046801 (2020).
58. Wei, Y. et al. A rhombohedral ferroelectric phase in epitaxially strained $Hf_{0.5}Zr_{0.5}O_2$ thin films. *Nature Mater.* **17**, 1095 (2018).
59. Ibañez-Azpiroz, J., Tsirkin, S. S. & Souza, I. Ab initio calculation of the shift photocurrent by wannier interpolation. *Phys. Rev. B* **97**, 245143 (2018).
60. Wang, C. et al. First-principles calculation of nonlinear optical responses by wannier interpolation. *Phys. Rev. B* **96**, 115147 (2017).
61. Giannozzi, P. et al. QUANTUM ESPRESSO: a modular and open-source software project for quantum simulations of materials. *J. Phys. Condens. Matter* **21**, 395502 (2009).
62. Giannozzi, P. et al. Advanced capabilities for materials modelling with QUANTUM ESPRESSO. *J. Phys. Condens. Matter* **29**, 465901 (2017).
63. Garrity, K. F., Bennett, J. W., Rabe, K. M. & Vanderbilt, D. Pseudopotentials for high-throughput DFT calculations. *Comput. Mater. Sci.* **81**, 446 (2014).
64. Perdew, J. P., Burke, K. & Ernzerhof, M. Generalized gradient approximation made simple. *Phys. Rev. Lett.* **77**, 3865 (1996).
65. Pizzi, G. et al. Wannier90 as a community code: new features and applications. *J. Phys. Condens. Matter.* **32**, 165902 (2020).

66. van Setten, M. et al. The PseudoDojo: Training and grading a 85 element optimized norm-conserving pseudopotential table. *Comput. Phys. Commun.* **226**, 39 (2018).
67. Krukau, A. V., Vydrov, O. A., Izmaylov, A. F. & Scuseria, G. E. Influence of the exchange screening parameter on the performance of screened hybrid functionals. *J. Chem. Phys.* **125**, 224106 (2006).
68. Marzari, N., Mostofi, A. A., Yates, J. R., Souza, I. & Vanderbilt, D. Maximally localized wannier functions: Theory and applications. *Rev. Mod. Phys.* **84**, 1419 (2012).
69. Tsirkin, S. S. High performance wannier interpolation of berry curvature and related quantities with WannierBerri code. *npj Comput. Mater.* **7**, 33 (2021).
70. Destraz, D. et al. Magnetism and anomalous transport in the weyl semimetal PrAlGe: possible route to axial gauge fields. *npj Quant. Mater.* **5**, 5 (2020).

ACKNOWLEDGEMENTS

Z.Q. and S.L. acknowledge the supports from Westlake Education Foundation. We acknowledge Dr. Jae-Mo Lihm for useful suggestions regarding the usage of Wannier90 and Wannier Berri. Z.Q. acknowledges the help from Yudi Yang during the preparation of the manuscript. The computational resource is provided by Westlake HPC Center. J.Z. acknowledges National Natural Science Foundation of China under Grant No. 11974270.

AUTHOR CONTRIBUTIONS

S.L. conceived and led the project. Z.Q. performed calculations and data analysis. All authors contributed to the discussion and the manuscript preparation.

COMPETING INTERESTS

The author declares no competing interests.

ADDITIONAL INFORMATION

Correspondence and requests for materials should be addressed to Shi Liu.

Reprints and permission information is available at http://www.nature.com/reprints

Publisher's note Springer Nature remains neutral with regard to jurisdictional claims in published maps and institutional affiliations.